



Lithium-ion battery degradation: Comprehensive cycle ageing data and analysis for commercial 21700 cells



Niall Kirkaldy ^{a,b,**}, Mohammad A. Samieian ^{a,b}, Gregory J. Offer ^{a,b}, Monica Marinescu ^{a,b}, Yatish Patel ^{a,b,*}

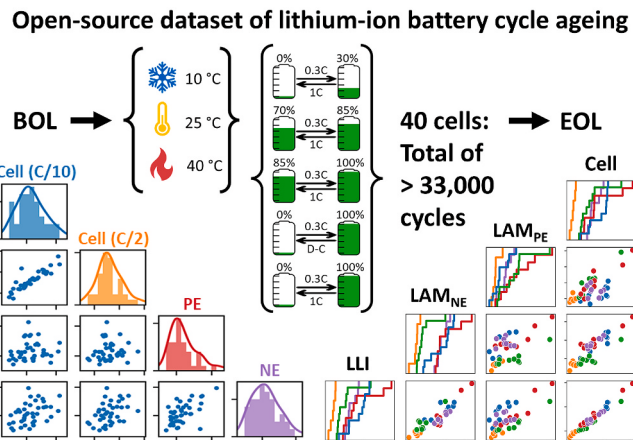
^a Mechanical Engineering Department, Imperial College London, UK

^b The Faraday Institution, Harwell Science and Innovation Campus, Didcot, UK

HIGHLIGHTS

- Open-source dataset for cycle ageing of commercial 21700 lithium-ion cells (LG M50T).
- 15 operating conditions of temperature and state of charge, probing different degradation mechanisms.
- Analysis includes quantified degradation modes of loss of active material and loss of lithium inventory.

GRAPHICAL ABSTRACT



ARTICLE INFO

Keywords:
Batteries
Lithium-ion
Degradation
Ageing
Lifetime
Data

ABSTRACT

High quality open-source battery data is in short supply and high demand. Researchers from academia and industry rely on experimental data for parameterisation and validation of battery models, but experimental data can be expensive and time consuming to acquire, and difficult to analyse without expert knowledge. Here we present a comprehensive open-source dataset for the cycle ageing of a commercially relevant lithium-ion cell (LG M50T 21700) with an NMC811 cathode and C/SiO_x composite anode. 40 cells were cycled over 15 different operating conditions of temperature and state of charge, accumulating a total of around 33,000 equivalent full cycles. Analysis of the ageing behaviour includes metrics such as capacity fade, resistance increase, and degradation mode analysis. The presentation of the dataset here is complemented by a statistical analysis of the cell performance, both at beginning of life and as a function of age. This provides a valuable resource for those working on battery performance and ageing.

* Corresponding author. Mechanical Engineering Department, Imperial College London, UK.

** Corresponding author. Mechanical Engineering Department, Imperial College London, UK.

E-mail addresses: n.kirkaldy@imperial.ac.uk (N. Kirkaldy), yatish.patel@imperial.ac.uk (Y. Patel).

1. Introduction

The battery industry is growing at an exceptional rate and is expected to quadruple in the next decade [1]. Demands from consumers are pushing the industry to make advancement to develop more capable batteries. Experimental data plays a vital role in progressing the advancements. Manufacturers that develop battery products rely on experimental data. Even with developments in modelling techniques, the models are only as accurate as the experimental data used for their parameterisation. We believe by having datasets publicly available, it will result in key contributions by experts in the field and hence lead to faster developments.

Many experimental research articles in the field of batteries generally only publish limited data, often limited to the particular storyline of that article [2–4]. Whilst this is useful for conveying a message to the battery community, it does not allow the reader to become aware of the bigger picture offered by a wider set of experimental data. Availability of a whole dataset allows the reader to make an independent interpretation and deduce conclusions which may have been overseen by the authors.

From an application point-of-view, availability of datasets can be useful to designers selecting batteries for products. Designers can make decisions about battery operating conditions and suitability of a cell in an application without conducting costly, long-term experiments.

Furthermore, whole datasets provide invaluable information to the wider battery community – beyond experimentalists. Datasets can be used for parameterising and validating battery models. Publicly available datasets will enable modellers to make advancements without relying on costs associated with gathering data experimentally [5] and without access to a laboratory. An example can be found from models developed [6,7] based on datasets published by NASA on 18650 cells – currently with 36000 views [8].

Recently there is a very high interest from outside the battery community to contribute to developments within the battery field. Experts in machine learning (ML) and artificial intelligence (AI) are eager to gain access to battery datasets [9]. In most cases they will not have access to battery testing laboratories. Machine learning tools could be used to significantly reduce costs in determining new materials for batteries [10, 11], provided substantial data is used to train the models. There are a very limited number of datasets which are publicly available [3,12–20]. Work has recently been done to gather and review available datasets [21], where various categories of battery data were reviewed, such as data required for model parametrisation and degradation data.

In this article we aim to give the readers access to all our experimental data for an ageing study done on 40 LG-M50T 21700 cylindrical cells. We have included details about both the ageing data and the reference performance tests (RPTs) along with their corresponding experimental data. We have also included plots to demonstrate some of the key findings and to give a general overview. The readers, however, should not be limited by our interpretation and can make independent interpretation of the experiments by plotting the raw data that is associated with this publication.

2. Experimental

2.1. Experimental setup

40 commercial 21700 cylindrical cells (LG M50T, LG GBM50T2170) were tested in this study. The LG M50T cell has a $\text{LiNi}_{0.8}\text{Mn}_{0.1}\text{Co}_{0.1}\text{O}_2$ (NMC811) positive electrode and C/SiO_x (herein referred to as Gr for graphite and Si for SiO_x) composite negative electrode, and has previously been thoroughly characterised by Chen et al. [22] 40 cells were cycle aged under 3 different temperatures [10, 25, 40] °C and 4 different state of charge (SoC) ranges [0–30, 70–85, 85–100, 0–100]%, as well as a further [0–100]% SoC range experiment which utilised a drive-cycle discharge instead of constant-current (CC). The same C-rates were used in all tests. Multiple cells were tested under each condition, with a

minimum of 2 cells, but in most cases 3 cells. Full details are shown in Table 1.

Cells were base-cooled at set temperatures using bespoke test rigs (full details in our previous publication) [2]. Cells were electrochemically cycled as detailed in Sections 2.3 and 2.4 using a Biologic BCS-815 battery cycler. Cells were subject to break-in cycles (section 2.2) prior to beginning of life (BoL) performance tests using the ‘Reference Performance Test’ (RPT) procedures (section 2.4). They were then alternately subject to ageing sets (section 2.3.1) and RPTs until the end of testing.

2.2. Break-in cycles

Prior to any ageing or performance checks, all cells were subject to 5 full charge-discharge cycles as part of the break-in procedure. This consisted of a 0.2C charge to 4.2 V with CV-hold until C/100, and 0.2C discharge to 2.5 V. Cells were rested under open circuit conditions for 2 h after each charge and 4 h after each discharge. These break-in cycles were performed at 25 °C for all cells.

2.3. Ageing conditions

The data is split into 5 ‘experiments’, which correspond to the different SoC windows (or discharge type) of the different ageing conditions. Each of these experiments contains data from cells aged at 3 different temperatures; the same 3 temperature set-points were used in all experiments. The SoC windows were chosen to degrade the cells in certain ways: we hypothesised that cycling at 0–30% SoC would cause an increased rate of degradation for the silicon within the negative electrode, since this is most active at low cell SoCs; 70–85% SoC was expected to cause mainly solid electrolyte interphase (SEI) growth, with limited effects from other mechanisms; 85–100% SoC was expected to result in lithium plating at low temperatures, and increased positive electrode decomposition at high temperatures. All mechanisms were expected to contribute to degradation for the 0–100% SoC range, while the 0–100% SoC drive-cycles provided a use-case closer to real applications.

All cells were aged using the same C-rates of 0.3C (charge) and 1C (discharge), with the exception of experiment 4, which uses a drive-cycle discharge based on the Worldwide harmonised Light vehicle Test Protocol (WLTP) drive cycle (i.e., noisy current). This WLTP drive cycle was adapted from Ref. [23] by scaling by the nominal cell capacities.

An ‘ageing set’ was defined by a set number of ageing cycles that the cell is subject to between RPTs. The number of cycles per ageing set was scaled according to the size of the SoC window, resulting in a similar number of equivalent full cycles in each ageing set (and therefore

Table 1

Summary of the cycle ageing study, showing conditions used and distribution of cells.

Experiment	SoC window	Cycles per ageing set	Current	Temperature	Number of cells
1	0–30%	258	0.3C/1C	10 °C	3
				25 °C	3
				40 °C	3
2	70–85%	515	0.3C/1C	10 °C	2
				25 °C	2
				40 °C	2
3	85–100%	515	0.3C/1C	10 °C	3
				25 °C	3
				40 °C	3
4	0–100% (drive-cycle)	78	0.3C/noisy C	10 °C	3
				25 °C	2
				40 °C	3
5	0–100%	78	0.3C/1C	10 °C	3
				25 °C	2
				40 °C	3

between RPTs). i.e., the 0–30% SoC window is approx. 0.3 times the size of the 0–100% SoC window, so the cells aged in this condition underwent 1/0.3 times as many cycles in each ageing set compared to the 0–100% SoC condition ($78/0.3 \approx 258$).

2.3.1. Ageing procedures

Tables 2–6 detail the specific procedures used for the ageing cycles. The white boxes indicate steps which bring the cell to the initial state where cycling can begin; this involved taking the cell to the required starting SoC for the ageing cycles, before bringing them to the desired set-point temperature. The temperature change was performed during the final rest period prior to the ageing cycles commencing. In all cases, cells were rested for a total of 4 h during this initial section.

For all of these experiments, the capacity used for SoC calculation is not updated as the cell degrades, and was always based on the BoL value of 4.865 Ah (corresponding to the mean C/10 discharge capacity from a subset of 20 cells). Derating the capacity for SoC and C-rate definition can extend the lifetime of cells [24]; however, this was not the aim of the current study, and so was not implemented here. For experiments which require control over the amount of charge passed (Expts. 1, 2 & 3), ΔQ limits were set on the battery cycler control software; experiments 4 & 5 did not require ΔQ limits since they are full depth-of-discharge tests which only rely on the voltage limits of the cell. Secondary safety limits were enabled for safety reasons and were not normally activated. For all experiments, there was a further temperature safety limit of 60 °C (not listed in the tables below). This limit was never triggered in any of the cases.

2.4. Reference performance tests (RPTs)

All cells were characterised at BoL and after each ageing set using a reference performance test (RPT). The RPT was always performed at 25 °C. Two different RPT procedures were used alternately: a longer procedure which was performed after each even-numbered ageing set, and a shorter procedure which was used after each odd-numbered ageing set. Both procedures are summarised below, and shown graphically in Fig. 1c. A CC-CV charge at 0.3C to 4.2 V, 4.2 V until C/100 (and subsequent 1 h rest) was performed before each individual step of the procedures.

2.4.1. Summary of the long RPT procedure

1. C/10 discharge-charge cycle between the voltage limits (2.5 V and 4.2 V).
2. C/2 discharge-charge cycle between the voltage limits (2.5 V and 4.2 V).
3. Galvanostatic intermittent titration technique (GITT) discharge at 0.5C; 25 pulses with each pulse passing 200 mAh of charge, with 1 h rest between pulses; lower cut-off voltage of 2.5 V (but continued test for all pulses).
4. GITT discharge at 0.5C; 5 pulses with each pulse passing 1000 mAh of charge, with 1 h rest between pulses; lower cut-off voltage of 2.5 V (but continued test for all pulses).

Table 2

Cycling procedure used in experiment 1 (0–30% SoC cycling).

Step	Control Type	Control Value	Primary Limits
1	CC discharge	1C	$E_{cell} = 2.5$ V
2	CV discharge	2.5 V	$ I < C/100$
3	Rest	Rest at OCV	time = 4 h
4	CC charge	0.3C	$Q = 1500$ mAh (=capacity ^a × 0.3)
5	CC discharge	1C	$E_{cell} = 2.5$ V
6	Loop to step 4	N/A	257 times

^a The capacity in this experiment was set to nominal capacity of 5 Ah instead of the measured value from beginning of life characterisation (4.865 Ah). This makes the actual SoC window 0–30.8% instead of 0–30%.

Table 3

Cycling procedure used in experiment 2 (70–85% SoC cycling).

Step	Control Type	Control Value	Primary Limits
1	CC charge	0.3C	$E_{cell} = 4.2$ V
2	CV charge	4.2 V	$ I < C/100$
3	Rest	Rest at OCV	time = 1 h
4	CC discharge	1C	$Q = 730$ mAh (=capacity ^a × 0.15)
5	Rest	Rest at OCV	time = 3 h
6	CC discharge	1C	$Q = 730$ mAh (=capacity ^a × 0.15)
7	CC charge	0.3C	$Q = 730$ mAh (=capacity ^a × 0.15)
8	Loop to step 6	N/A	514 times

^a The capacity used in these calculations is 4.865 Ah (from BoL characterisation).

Table 4

Cycling procedure used in experiment 3 (85–100% SoC cycling).

Step	Control Type	Control Value	Primary Limits
1	CC charge	0.3C	$E_{cell} = 4.2$ V
2	CV charge	4.2 V	$ I < C/100$
3	Rest	Rest at OCV	time = 4 h
4	CC discharge	1C	$Q = 730$ mAh (=capacity ^a × 0.15)
5	CC charge	0.3C	$E_{cell} = 4.2$ V
6	CV charge	4.2 V	$ I < C/100$
7	Loop to step 4	N/A	514 times

^a The capacity used in these calculations is 4.865 Ah (from BoL characterisation).

Table 5

Cycling procedure used in experiment 4 (drive cycles, full depth-of-discharge).

Step	Control Type	Control Value	Primary Limits
1	CC charge	0.3C	$E_{cell} = 4.2$ V
2	CV charge	4.2 V	$ I < C/100$
3	Rest	Rest at OCV	time = 4 h
4	CC discharge	1C	250 mAh
5	Drivecycle discharge (WLTP repeated until primary limit reached)	Variable current	$E_{cell} = 2.5$ V
6	CC charge	0.3C	$E_{cell} = 4.2$ V
7	CV charge	4.2 V	$ I < C/100$
8	Loop to step 4	N/A	77 times

*A brief CC discharge was performed prior to the drive cycle due to some charging current near the beginning of the drive cycle current vs time profile, which would potentially cause the cell voltage to accidentally go above 4.2 V.

Table 6

Cycling procedure used in experiment 5 (constant current cycling, full depth-of-discharge).

Step	Control Type	Control Value	Primary Limits
1	CC charge	0.3C	$E_{cell} = 4.2$ V
2	CV charge	4.2 V	$ I < C/100$
3	Rest	Rest at OCV	time = 4 h
4	CC discharge	1C	$E_{cell} = 2.5$ V
5	CC charge	0.3C	$E_{cell} = 4.2$ V
6	CV charge	4.2 V	$ I < C/100$
7	Loop to step 4	N/A	77 times

2.4.2. Summary of the short RPT procedure

1. C/10 discharge-charge cycle between the voltage limits (2.5 V and 4.2 V).
2. Pulse-under-load test with average current of C/2: A baseline DC current of C/2 was applied with a hybrid pulse power characterisation (HPPC)-type profile superimposed on top (hereby termed pulse-under-load, PUL). This was done for discharge and charge (with voltage limits of 2.5 V and 4.2 V).

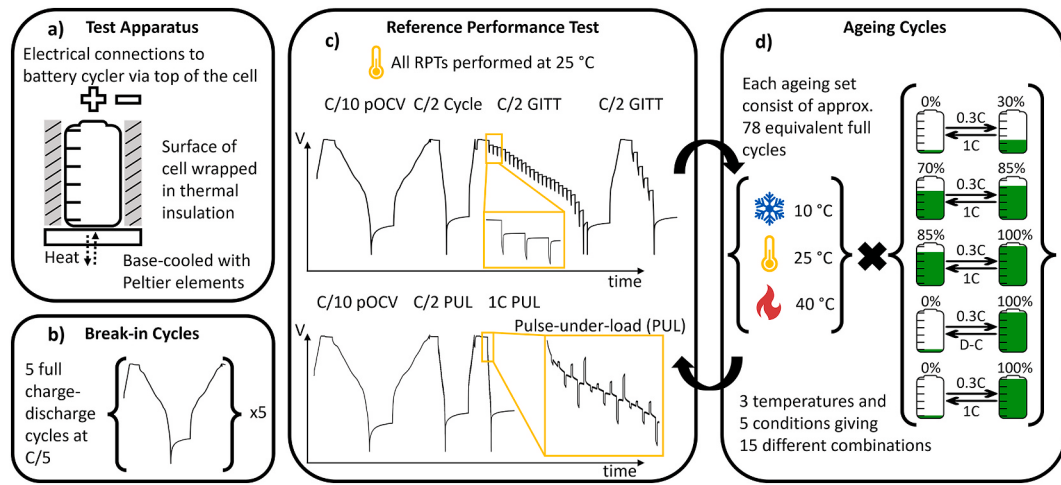


Fig. 1. Schematic representation of the experimental methods. a) Test apparatus: cells were base-cooled using bespoke test rigs, with electrical connections via the top of the cell. b) Break-in cycles: cells were subject to 5 full charge-discharge cycles at C/5 prior to any other testing. c) Reference performance tests (RPTs): cells were subject to RPTs at beginning of life and after each ageing set; 2 different procedures were used alternately, with a longer procedure (top) and a shorter procedure (bottom). d) Ageing Cycles: cells were aged under 15 different conditions, consisting of different temperature set-points, SoC ranges, and discharge procedures (constant current or drive-cycle (D-C)).

3. PUL test with average current of 1C. A baseline DC current of 1C was applied with an HPPC-type profile superimposed on top. This was done for discharge only (with a voltage limit of 2.5 V).

3. Results & discussion

3.1. Beginning of life

The BoL performance of all 40 cells is compiled in Fig. 2. Voltage vs discharge capacity plots (Fig. 2a) show only minor cell-to-cell variations (the displayed data is an overlay of all 40 cells) for each of the segments of the longer RPT procedure. C/10 and C/2 cell discharge capacities were directly determined from these measurements; cell resistance was calculated from the 25-pulse GITT data (Fig. 2b) as described below; active-material-level capacities and electrode offsets were determined via open circuit voltage (OCV) fitting (method shown in Fig. 3); distributions for and correlations between each variable are shown in Fig. 4.

The mean C/10 and C/2 cell discharge capacities were found to be 4.857 Ah and 4.780 Ah, with standard deviations (std) of 0.022 Ah and 0.022 Ah, respectively. This constitutes a very low coefficient of variation of 0.45% for cell capacity.

The cell-to-cell variation in resistance was found to be higher than that in capacity. Calculating cell resistance from the voltage drop upon application of current during the pulsed discharge of the 25-pulse GITT resulted in the plots shown in Fig. 2b. The sampling rate during the GITT pulses was 10 Hz, giving a maximum resolution of 0.1 s for resistance determination. Comparing the 0.1 s resistance ($R_{0.1s}$) of all cells at 52% SoC (i.e. during the 12th pulse of the GITT procedure) reveals a mean value of 26.42 mΩ, with a std of 0.78 mΩ (2.95%). Similarly, calculating the resistance 10 s (R_{10s}) after application of current gave a mean of 32.96 mΩ and std of 0.79 mΩ (2.40%). However, by subtracting $R_{0.1s}$ from R_{10s} , the coefficient of variation is reduced to 1.68% (6.54 mΩ mean, 0.11 mΩ std). The instantaneous voltage drop in lithium-ion batteries is attributed to purely ohmic resistances, while the voltage

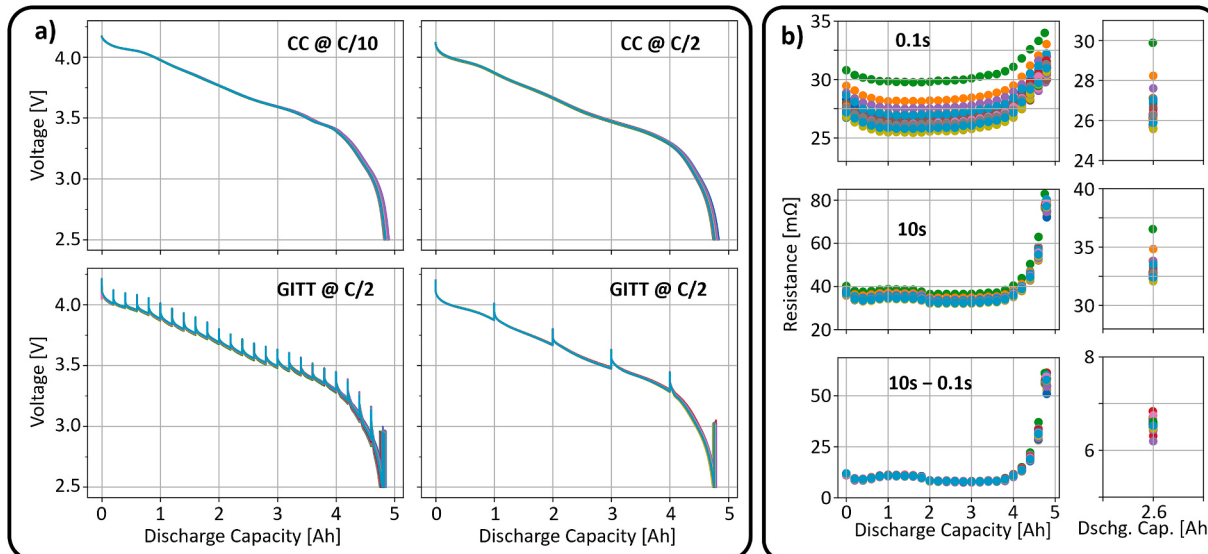


Fig. 2. Beginning of life performance of 40 LG M50T cells. a) Voltage vs discharge capacity plots of the four subtests of the longer RPT procedure, showing data from 40 cells overlaid. b) Calculated cell resistance as a function of discharge capacity at different timescales from GITT data, showing $R_{0.1s}$ (top), R_{10s} (middle), and $R_{10s-0.1s}$ (bottom); plots on the right show a zoomed-in view of the resistance at the 12th pulse of the GITT procedure (~52% SoC).

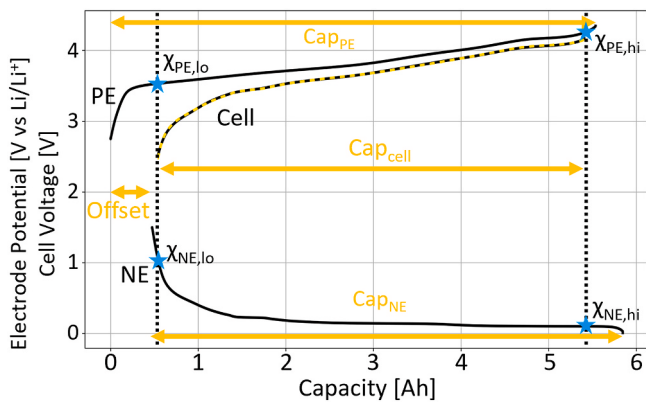


Fig. 3. Example of OCV-fitting to determine electrode-level capacities and degradation modes. Experimentally measured cell voltage vs capacity (black) and simulated cell capacity (yellow dashed), alongside positive and negative electrode voltage curves; vertical dashed lines and blue stars show the upper/lower limits of each electrode when the cell is fully charged/discharged. (For interpretation of the references to colour in this figure legend, the reader is referred to the Web version of this article.)

drop over longer time periods is impacted by other resistance contributions from charge transfer reactions and mass transport effects. The larger variance of R_{0.1s} is due to the impact of the electrical connections between the battery cycler and the cell. The battery cycler connections are only 4-point measurements as far as the ring/pin terminals which connect the banana plugs to the cell casing. The measured resistance therefore also includes the ohmic resistance of these connections. However, by subtracting R_{0.1s} from R_{10s}, the effect of the electrical

connections is removed from the resistance measurement. Care was taken on setup of the test apparatus to minimise these resistances, but their impact is still visible in the resultant data, as evidenced by the outliers in R_{0.1s} and R_{10s} shown in the histograms on the upper right of Fig. 4.

Electrode- and active material-level capacities can be determined using OCV-fitting methods (Fig. 3) such as that detailed in our previous work and elsewhere [2,25–27]. These methods utilise experimentally measured half-cell V vs Q curves to simulate a full-cell V vs Q curve. Altering the operating ranges (upper/lower lithiation limits, highlighted by the blue stars in Fig. 3) of each electrode results in changes to the simulated full-cell V vs Q curve. An optimisation function varies these operating ranges such that the difference between the simulated full-cell V vs Q curve and an experimentally measured full-cell V vs Q curve (from C/10 discharge) is minimised. The resulting operating ranges can be used alongside the experimentally measured full-cell capacity to calculate electrode capacities. For composite electrodes, such as the silicon-graphite negative electrode of the LG M50T cell used in this study, capacities can be determined for each component/active material in the composite. This is possible due to the fact that the composite Q vs V curve is the sum of those of the constituent materials. We used reference OCV profiles for graphite, silicon, and the NMC811 positive electrode materials taken from the literature [22,26,28].

It is worth noting that the calculated capacities may not constitute the entire capacity of the active material, rather they represent the useable capacity over the voltage range that we have half-cell data for. That is, if there is additional capacity outside of the measured voltage range of the electrode material, it is not included in the calculated values. For full details of the fitting method, see our previous work [2].

Histograms for the cell and active-material capacities are shown in

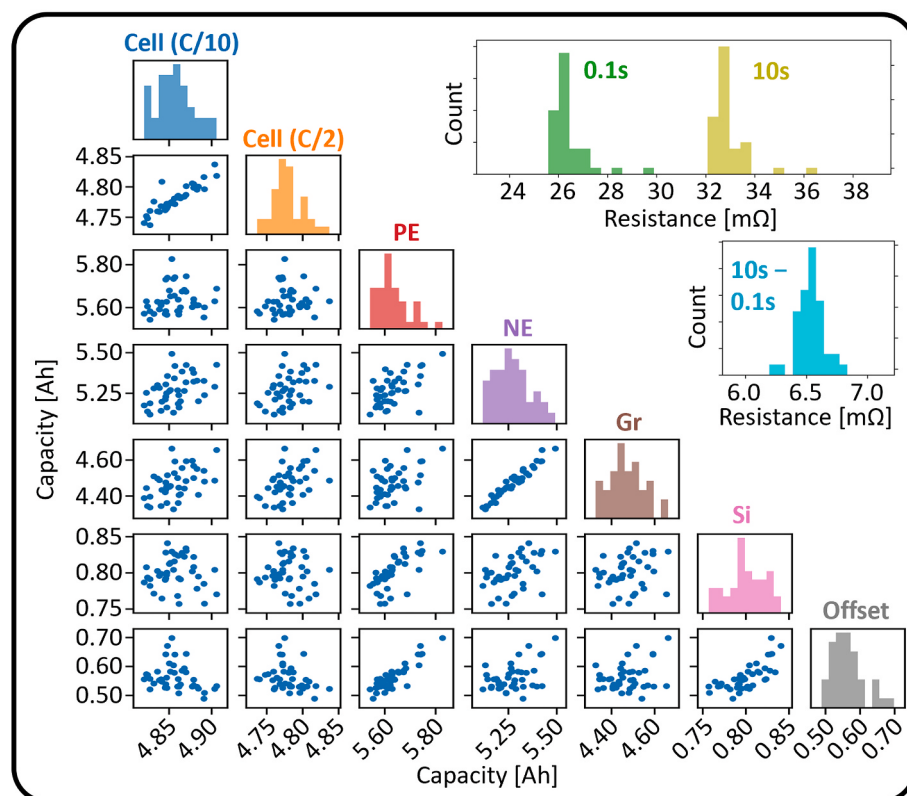


Fig. 4. Histograms and correlation matrix for the cell- and electrode-level capacities and offset (lower left), and histograms for cell resistances at different timescales at ~52% SoC (upper right). Capacities and offsets were determined from OCV-fitting of the C/10 discharge data; resistances were calculated from the C/2 GITT data. Abbreviations shown are, “Cell (C/10)”: C/10 discharge capacity of the cell; “Cell (C/2)”: C/2 discharge capacity of the cell; “PE”: positive electrode capacity; “NE”: negative electrode capacity; “Gr” capacity of graphite in the negative electrode; “Si”: capacity of silicon in the negative electrode; “Offset”: offset between electrodes as shown diagrammatically in Fig. 3. (For interpretation of the references to colour in this figure legend, the reader is referred to the Web version of this article.)

Fig. 4 (diagonal), alongside a correlation matrix. The capacities of the electrodes and active materials are shown in **Table 7**, alongside cell level capacities and resistances. Strong correlations were observed between cell C/10 and cell C/2 capacities, and between the negative electrode and graphite capacities. This is expected, since these pairs of variables are fundamentally coupled. A weaker correlation between positive electrode capacity and electrode offset was also observed; this could be an after effect of the formation process.

3.2. Cycle ageing

After BoL characterisation, cells were subject to ageing sets as described in section 2.3. Each ageing set consisted of a set number of cycles which equated to approximately 78 full equivalent cycles. After each ageing set, an RPT was performed to characterise performance. **Fig. 5** shows data extracted from the ageing sets themselves for two of the five SoC ranges; these metrics are the average from each set, showing charge (Q) and energy (E) passed, average voltage (V_{av}), voltage range (V_{range}), and average temperature (T_{av}). It should be noted that plots share common scales for Q , E , and T_{av} , but have separate scales for V_{av} and V_{range} .

For experiments which involved coulomb-counting, such as the 85–100% SoC range shown on the left of **Fig. 5**, the values of charge (Q) and energy (E) passed can be seen to remain constant, until hitting a cliff-edge in some cases. Meanwhile, the voltage range (V_{range}) can be seen to gradually increase. This is due to the operating voltage window needing to increase to pass the same amount of charge as the capacity of the cell decreases, and because the cell resistance increases. Once V_{range} equals the full operating voltage range of the cell (1.7 V), Q and E can be seen to rapidly decrease, since the cells are effectively now being cycled over their full useable SoC range.

Conversely, in the full depth-of-discharge (DoD) experiments (including the drive-cycle discharge shown on the right of **Fig. 5**), V_{range} is relatively constant at 1.7 V (equalling the difference between the upper and lower voltage limits of 4.2 V and 2.5 V). However, Q and E both decrease with age, since the capacity of the cell decreases and the resistance increases.

Cells were base-cooled during cycling, with set-point temperatures of 10, 25, and 40 °C for the cooling-block at the base of the cell. The surface temperatures of the cells were measured using K-type thermocouples approximately half way up the height of the can. The average surface temperature (T_{av}) measured for each cell during each ageing set was found to be relatively constant throughout. Average cell surface temperatures were generally higher than the set-point temperatures of the test apparatus due to heat generation during cycling. The elevated cell temperature is more pronounced for cells aged at lower set-point temperatures, since cell resistances are larger and therefore heat generation is greater. The method of base-cooling cells therefore provides an effective means of maintaining a constant cell surface temperature during cycling, in part due to higher rates of heat transfer through

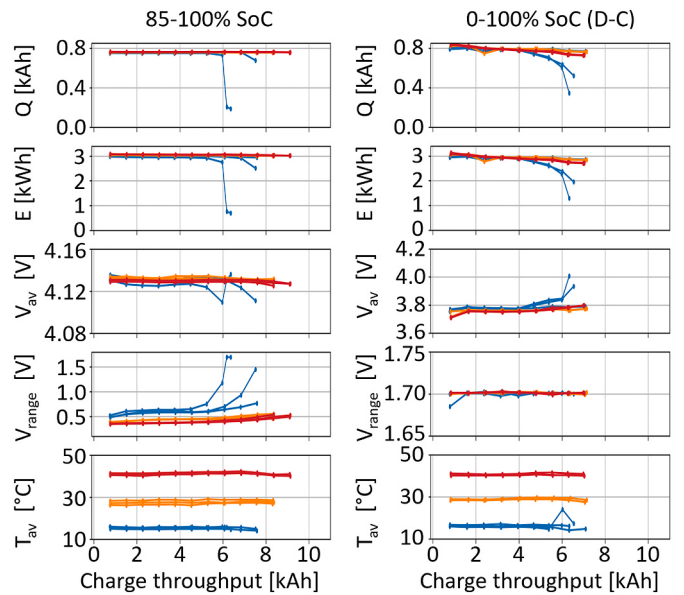


Fig. 5. Data extracted from the ageing cycles, showing charge (Q) and energy (E) passed, average voltage (V_{av}), voltage range (V_{range}), and average temperature (T_{av}). The colours in the plots correspond to the ageing set point temperatures of 10 (blue), 25 (orange), and 40 °C (red). The left column of plots corresponds to cells cycled at 85–100% SoC, and those on the right correspond to cells cycled at 0–100% SoC with a drive-cycle discharge. (For interpretation of the references to colour in this figure legend, the reader is referred to the Web version of this article.)

conduction compared to convection of air-cooled cells [29].

3.3. RPT data

The RPT data gives higher quality information on the ageing behaviour of the cells. Two RPT procedures were used in this study, which alternated between ageing sets. Both versions of the RPT procedure contained a C/10 discharge-charge cycle, which was used for determining cell-level capacity fade, and also used as pseudo-OCV data for degradation mode analysis (DMA) as described in our previous work [2]. The longer RPT procedure was performed after each even-numbered ageing set, and contained GITT tests which were used for determining the resistance increase during ageing. This RPT procedure also contained a C/2 discharge-charge cycle and a GITT with longer duration pulses, which give information on useable capacity and longer time-constant processes during operation, respectively. The shorter RPT procedure instead contained two pulse-under-load (PUL) tests, which can be used for updating parameters for equivalent circuit models as a function of age and for determining various resistance contributions.

Voltage vs capacity plots of some of the RPT subtests are shown for a single example cell in **Fig. 6a-d**. This cell was aged by cycling over the 0–100% SoC range at 25 °C. The plots reveal how the voltage profiles change as a function of charge throughput from the ageing cycles, indicated by the colour bar on the right. Similarly, resistance vs capacity profiles were determined through analysis of the GITT data as described in section 3.1; an example of the resulting R vs Q profiles as a function of age for a single cell is shown in **Fig. 6e** and f.

Ageing metrics determined from the RPT data are shown in **Fig. 7** as a function of charge throughput for each of the 40 cells tested. Alongside traditional metrics of capacity fade (C.F) and resistance increase (RI), degradation modes of loss of active material (LAM) of the positive and negative electrodes (PE and NE) and graphite and silicon (Gr and Si) active materials in the negative electrode, and loss of lithium inventory (LLI) were also calculated.

Table 7
Beginning of life values for various performance metrics averaged over 40 cells.

Variable	Mean value	Standard deviation	Coefficient of variation (%)
Cell (C/10) capacity	4.857 Ah	0.022 Ah	0.45
Cell (C/2) capacity	4.780 Ah	0.022 Ah	0.46
Positive electrode capacity	5.634 Ah	0.064 Ah	1.14
Negative electrode capacity	5.272 Ah	0.092 Ah	1.75
Graphite capacity	4.471 Ah	0.085 Ah	1.90
Silicon capacity	0.800 Ah	0.022 Ah	2.75
Offset	0.563 Ah	0.046 Ah	8.17
$R_{0.1s}$	26.42 mΩ	0.78 mΩ	2.95
R_{10s}	32.96 mΩ	0.79 mΩ	2.40
$R_{10s-0.1s}$	6.54 mΩ	0.11 mΩ	1.68

From Fig. 7 it is clear that the ageing trajectories of the cells are usage-dependent. Degradation of cells cycled in the 70–85% SoC range is particularly slow, whereas those cycled in the SoC extremes (0–30% and 85–100%) are seen to degrade at faster rates. There are also stark differences in cells aged under constant current cycling versus those undergoing drive-cycle discharge (both in the 0–100% SoC range), in particular when operating in cold conditions (10 °C). Cold conditions also result in greater capacity fade in cells cycled in the high 85–100% SoC range compared to warmer temperatures; this is likely due to lithium-plating on the negative electrode.

Interestingly, some capacity recovery can be observed for one of the cells aged under these conditions (85–100% SoC at 10 °C, shown on the left of Fig. 7), as evidenced by the final datapoint for that cell. It is important to note that the final RPT which displayed this capacity recovery was performed after an extended period after cycling finishing (23 days between the final ageing set finishing and the final RPT commencing). The recovery is not only evident in the measured cell capacity, but also the shape of the pseudo-OCV curve of the cell. The OCV-fitting procedure used for degradation mode analysis was unable to accurately determine the electrode-level capacities in this case, giving a high root mean squared error.

Some cells were cycled until the “cliff-edge” or “knee-point” of degradation was observed, while others were stopped prior to this point due to resource limitations. All cells were subject to at least 8 ageing sets (9 RPTs including BoL). Aggregating data from all cells tested in each experiment allows empirical cumulative distribution functions (ECDFs) to be computed for each ageing metric. These are shown on the left of Fig. 8, with each row corresponding to an RPT and the colours of the ECDFs corresponding to the experiment (i.e. how the cells were aged). By separating the data in this way, it becomes clear which ageing metrics are affected most by each ageing condition. It should be noted that in these plots, the data are grouped by RPT number rather than amount of charge throughput during cycling; therefore some cells may have been cycled more than others. For RPTs higher than RPT8, some cells have been removed from testing, either due to reaching end-of-life or otherwise. As such, the sample size is smaller, and any especially degraded cells are not present in the analyses.

By taking data from RPT8 (the last RPT which was applied to all 40 cells), correlations between the ageing metrics were determined (right of Fig. 8). In this correlation matrix, data have been grouped by ageing temperature (bottom left half) and by experiment (top right half), with the diagonal showing ECDFs of each variable split by experiment.

Correlations are observed between fundamentally coupled metrics

such as C/10 capacity ($Q_{C/10}$) and C/2 capacity ($Q_{C/2}$), and losses of active material from the negative electrode (LAM_{NE}) and graphite (LAM_{Gr}). However, other correlations between independent variables are also observed, in particular between LLI and both cell- and NE-capacity. The correlation between LLI and cell capacity fade has been observed previously by Schmidt et al. [30], while the correlation between LLI and LAM_{NE} could indicate that the LAM at the negative electrode is from lithiated active material.

Clusterings of colour in Fig. 8 indicate condition-dependent ageing behaviour. In particular, it is clear that cycling in the 0–30% SoC range (blue markers on upper right corner of the matrix) is detrimental for silicon capacity but not as harmful for graphite capacity. Meanwhile cycling in the 70–85% SoC range (orange markers on upper right corner of the matrix) is generally the least destructive for the cell, evidenced by these datapoints being in the lower left corner of each plot. The temperature-dependence is less clear from the matrix, though cold temperatures (blue markers in the lower left corner of the matrix) often result in greater levels of degradation, as shown by these markers being closer to the upper right of each plot.

The data presented in these analyses is not exhaustive, with plenty of information left untouched within the wider dataset. While we cannot present this in its entirety within this publication, it is contained in the accompanying data stored in an open-source repository. We hope this will prove useful for researchers working on lithium-ion batteries and electrochemical energy storage, and may lead to further discoveries in the future.

4. Conclusions

We have presented a comprehensive dataset for the cycle ageing of 40 commercially relevant lithium-ion battery cells (LG M50T 21700). The cells were thermally managed via conduction through the base, which is a common method of cooling cylindrical cells in real-world applications. This is complemented with a statistical analysis of the cell performance at beginning of life and in-depth analysis of the degradation behaviour under different cycling conditions. The cell-to-cell variability in capacity and resistance at beginning of life was found to be relatively low, with coefficients of variation of 0.45% and 1.68% for C/10 capacity and 10s–1s resistance, respectively. Electrode-level metrics were determined by open circuit voltage fitting, giving capacities of 5.634 Ah and 5.272 Ah for the positive and negative electrodes, with the negative electrode capacity consisting of graphite (4.471 Ah) and silicon (0.800 Ah) active materials.

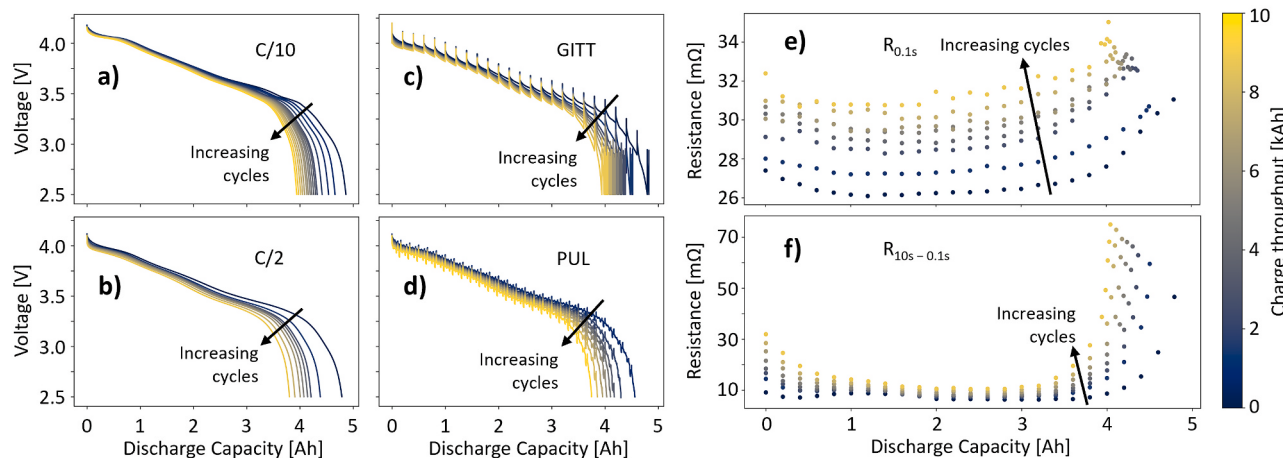


Fig. 6. Timeseries data for a single example cell, showing V vs Q plots for different subtests of the RPT procedures as a function of age: a) C/10 discharge, b) C/2 discharge, c) C/2 GITT, and d) C/2 PUL tests; resistance vs SoC plots as a function of age are shown in e) the 0.1s resistance, and f) the 10s–0.1s resistance. In all plots, the colour corresponds to the amount of charge throughput the cell has experienced at time of testing, with the colour bar legend shown on the right. (For interpretation of the references to colour in this figure legend, the reader is referred to the Web version of this article.)

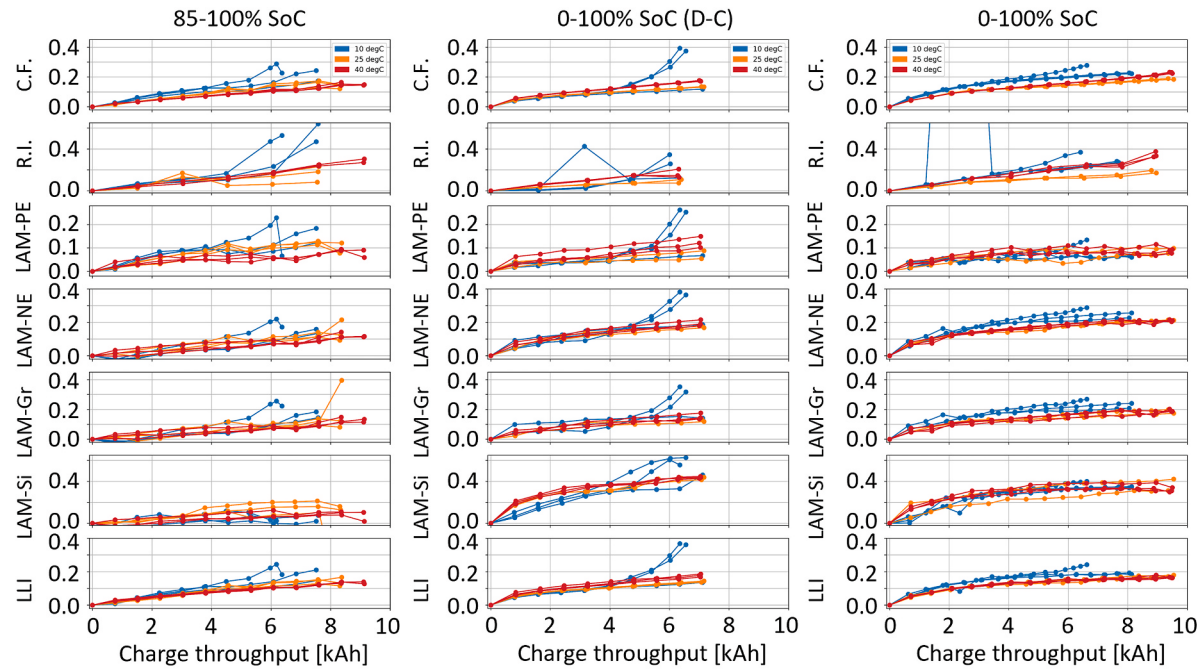


Fig. 7. Ageing metrics determined from the RPT data plotted as a function of charge throughput during cycle ageing. Data shown for cells cycled over the 85–100% SoC range (left), 0–100% SoC drive-cycle discharge (middle), and 0–100% CC discharge (right); colours correspond to the ageing temperatures of 10 °C (blue), 25 °C (orange), and 40 °C (red). Ageing metrics shown are capacity fade (“C.F.”), resistance increase (“R.I.”), loss of active material of the positive electrode (“LAM-PE”), negative electrode (“LAM-NE”), graphite (“LAM-Gr”), and silicon (“LAM-Si”), and loss of lithium inventory (“LLI”). (For interpretation of the references to colour in this figure legend, the reader is referred to the Web version of this article.)

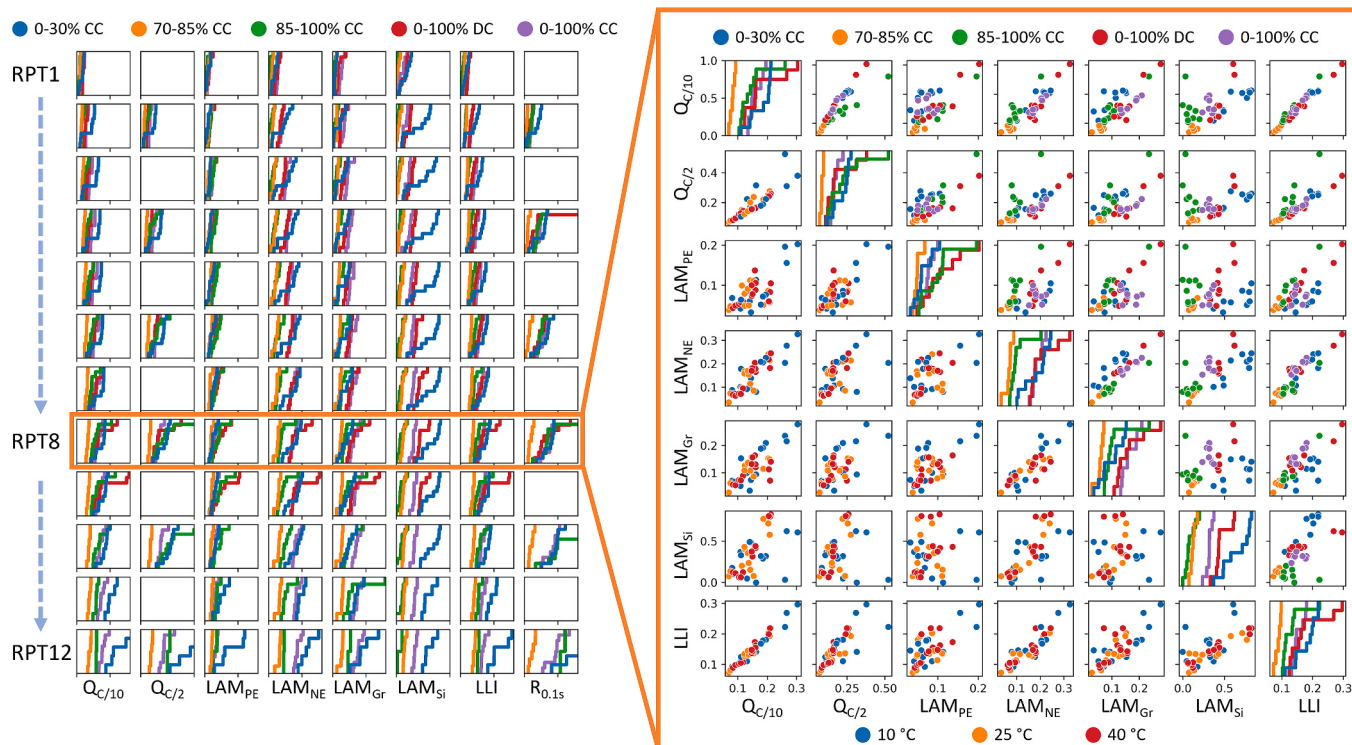


Fig. 8. Capacity fade, resistance increase, and DMs as function of age. Left: ECDF plots for various metrics, separated by experiment; each row represents all cells after a certain number of ageing sets, from RPT1 (top) to RPT12 (bottom). Some experiments/cells are only tested up to RPT8 (highlighted in orange box), with subsequent RPTs only showing data from the remaining cells under test. Right: Correlation matrix for all cells at RPT8, with ECDFs shown in the diagonal. The correlation plots in the top-right corner are separated by experiment (i.e. SoC range); those in the bottom-left corner are separated by temperature. (For interpretation of the references to colour in this figure legend, the reader is referred to the Web version of this article.)

Analysis of the degradation behaviour revealed stark differences in the ageing pathways of the different conditions. This is displayed in the plots of capacity fade and resistance increase as a function of charge throughput, but can be differentiated even more through comparing the degradation modes of loss of active material and loss of lithium inventory, which give degradation information on an electrode-level. Correlations between different degradation modes were observed in the data, and were further resolved through separating by ageing conditions.

The data presented here is openly available on the accompanying data repository on Zenodo. Care has been taken to curate the data according to the FAIR principles, making it an invaluable resource for battery researchers in a wide range of applications, from fundamental physics-based modelling to data science and beyond.

Data and code availability

All data supporting this study are openly available from Zenodo at <https://doi.org/10.5281/zenodo.10637534>. Code used in the analyses are available from GitHub at (<https://github.com/ImperialCollegeLondon/batteryDAT>).

CRediT authorship contribution statement

Niall Kirkaldy: Writing – review & editing, Writing – original draft, Visualization, Methodology, Investigation, Formal analysis, Data curation. **Mohammad A. Samieian:** Writing – original draft, Methodology, Investigation, Data curation. **Gregory J. Offer:** Writing – review & editing, Supervision, Funding acquisition, Conceptualization. **Monica Marinescu:** Writing – review & editing, Supervision, Project administration, Funding acquisition, Conceptualization. **Yatish Patel:** Writing – review & editing, Supervision, Methodology, Funding acquisition, Conceptualization.

Declaration of competing interest

The authors declare that they have no known competing financial interests or personal relationships that could have appeared to influence the work reported in this paper.

Data availability

The data is available for download from Zenodo at <https://doi.org/10.5281/zenodo.10637534>.

Acknowledgements

This work was kindly supported by the Innovate UK WIZer project (grant number 104427), the EPSRC Faraday Institution Multi-Scale Modelling project (<https://faraday.ac.uk/>; EP/S003053/1, grant number FIRG025).

Appendix A. Supplementary data

Supplementary data to this article can be found online at <https://doi.org/10.1016/j.jpowsour.2024.234185>.

References

- [1] Lithium-Ion Battery Market Report 2023-2033 - Visiongain.
- [2] N. Kirkaldy, M.A. Samieian, G.J. Offer, M. Marinescu, Y. Patel, Lithium-Ion battery degradation: measuring rapid loss of active silicon in silicon-graphite composite electrodes, *ACS Appl. Energy Mater.* 5 (2022) 13367–13376, <https://doi.org/10.1021/acsaem.2c02047>.
- [3] N. Kirkaldy, M.A. Samieian, G.J. Offer, M. Marinescu, Y. Patel, Data from: Lithium-Ion Battery Degradation: Measuring Rapid Loss of Active Silicon in Silicon-Graphite Composite Electrodes, Dataset on Zenodo, 2022, <https://doi.org/10.5281/ZENODO.7235858>.
- [4] M.A. Samieian, C.E. Garcia, L.B. Diaz, A. Hales, Y. Patel, G.J. Offer, Large scale immersion bath for isothermal testing of lithium-ion cells, *HardwareX* 12 (2022) e00359, <https://doi.org/10.1016/j.hjox.2022.e00359>.
- [5] M.A. Samieian, A. Hales, Y. Patel, A novel experimental technique for use in fast parameterisation of equivalent circuit models for lithium-ion batteries, *Batteries* 8 (2022) 125, <https://doi.org/10.3390/BATTERIES8090125>, 125 8 (2022).
- [6] M.B. Jamshidi, N. Alibeigi, A. Lalbakhsh, S. Roshani, An ANFIS approach to modeling a small satellite power source of NASA, in: Proc. 2019 IEEE 16th Int. Conf. Networking, Sens. Control, ICNSC 2019, 2019, pp. 459–464, <https://doi.org/10.1109/ICNSC.2019.8743333>.
- [7] B. Bole, C.S. Kulkarni, M. Daigle, Adaptation of an electrochemistry-based Li-ion battery model to account for deterioration observed under randomized use, <https://doi.org/10.36001/PHMCNF.2014.V611.2490>, 2014.
- [8] Li-ion Battery Aging Datasets, *NASA Open Data Portal*, 2010.
- [9] M. Aykol, P. Herring, A. Anapolksky, Machine learning for continuous innovation in battery technologies, *Nat. Rev. Mater.* 510 5 (2020) 725–727, <https://doi.org/10.1038/s41578-020-0216-y>, 2020.
- [10] L. Ward, M. Aykol, B. Blaiszik, I. Foster, B. Meredig, J. Saal, S. Suram, Strategies for accelerating the adoption of materials informatics, *MRS Bull.* 43 (2018) 683–689, <https://doi.org/10.1557/mrs.2018.204/FIGURES/1>.
- [11] A.D. Sendek, E.D. Cubuk, E.R. Antoniouk, G. Cheon, Y. Cui, E.J. Reed, Machine learning-assisted discovery of solid Li-ion conducting materials, *Chem. Mater.* 31 (2019) 342–352, https://doi.org/10.1021/ACS.CHEMMATER.8B03272/SUPPL_FILE/CM8B03272_SI_001.PDF.
- [12] L. Wildfeuer, A. Karger, D. Aygül, N. Wassiliadis, A. Jossen, M. Lienkamp, Experimental degradation study of a commercial lithium-ion battery, *J. Power Sources* 560 (2023) 232498, <https://doi.org/10.1016/j.jpowsour.2022.232498>.
- [13] K. Rumpf, M. Naumann, A. Jossen, Experimental investigation of parametric cell-to-cell variation and correlation based on 1100 commercial lithium-ion cells, *J. Energy Storage* 14 (2017) 224–243, <https://doi.org/10.1016/J.JEST.2017.09.010>.
- [14] M. Hassini, E. Redondo-Iglesias, P. Venet, Lithium-Ion battery data: from production to prediction, *Batteries* 9 (2023) 385, <https://doi.org/10.3390/BATTERIES9070385>, 385 9 (2023).
- [15] G. dos Reis, C. Strange, M. Yadav, S. Li, Lithium-ion battery data and where to find it, *AI* 5 (2021) 100081, <https://doi.org/10.1016/J.EGYAI.2021.100081>.
- [16] M. Rashid, M. Faraji-Niri, J. Sansom, M. Sheikh, D. Widanage, J. Marco, Dataset for rapid state of health estimation of lithium batteries using EIS and machine learning: training and validation, *Data Brief* 48 (2023) 109157, <https://doi.org/10.1016/J.DIB.2023.109157>.
- [17] G. Pozzato, A. Allam, S. Onori, Lithium-ion battery aging dataset based on electric vehicle real-driving profiles, *Data Brief* 41 (2022) 107995, <https://doi.org/10.1016/J.DIB.2022.107995>.
- [18] A. Bills, S. Sripad, L. Fredericks, M. Guttenberg, D. Charles, E. Frank, V. Viswanathan, A battery dataset for electric vertical takeoff and landing aircraft, *Sci. Data* 101 (10) (2023) 1–7, <https://doi.org/10.1038/s41597-023-02180-5>, 2023.
- [19] M. Naumann, Data for: Analysis and Modeling of Cycle Aging of a Commercial LiFePO₄/graphite Cell, vol. 1, 2021, <https://doi.org/10.17632/GHGYR25H8D.1>.
- [20] M. Naumann, Data for: Analysis and Modeling of Calendar Aging of a Commercial LiFePO₄/graphite Cell, vol. 1, 2021, <https://doi.org/10.17632/KXH42BFGTJ.1>.
- [21] S.A. Hasib, S. Islam, R.K. Chakraborty, M.J. Ryan, D.K. Saha, M.H. Ahamed, S. I. Moyeen, S.K. Das, M.F. Ali, M.R. Islam, T. Tasneem, F.R. Badal, A comprehensive review of available battery datasets, RUL prediction approaches, and advanced battery management, *IEEE Access* 9 (2021) 86166–86193, <https://doi.org/10.1109/ACCESS.2021.3089032>.
- [22] C.-H. Chen, F.B. Planella, K. O'Regan, D. Gastol, W.D. Widanage, E. Kendrick, Development of experimental techniques for parameterization of multi-scale lithium-ion battery models, *J. Electrochem. Soc.* 167 (2020) 80534, <https://doi.org/10.1149/1945-7111/ab9050>.
- [23] A. Hales, E. Brouillet, Z. Wang, B. Edwards, M.A. Samieian, J. Kay, S. Mores, D. Auger, Y. Patel, G. Offer, Isothermal temperature control for battery testing and battery model parameterization, *SAE Int. J. Electrified Veh* 10 (2021) 105–122, <https://doi.org/10.4271/14-10-02-0008>.
- [24] H. Ruan, J.V. Barreras, T. Engstrom, Y. Merla, R. Millar, B. Wu, Lithium-ion battery lifetime extension: a review of derating methods, *J. Power Sources* 563 (2023) 232805, <https://doi.org/10.1016/j.jpowsour.2023.232805>.
- [25] M. Dubarry, C. Truchot, B.Y. Liaw, Synthesize battery degradation modes via a diagnostic and prognostic model, *J. Power Sources* 219 (2012) 204–216, <https://doi.org/10.1016/J.JPOWSOUR.2012.07.016>.
- [26] R. Prosser, G. Offer, Y. Patel, Lithium-Ion diagnostics: the first quantitative in-operando technique for diagnosing lithium ion battery degradation modes under load with realistic thermal boundary conditions, *J. Electrochem. Soc.* 168 (2021) 030532, <https://doi.org/10.1149/1945-7111/abed28>.
- [27] J. Schmitt, M. Schindler, A. Oberbauer, A. Jossen, Determination of degradation modes of lithium-ion batteries considering aging-induced changes in the half-cell open-circuit potential curve of silicon-graphite, *J. Power Sources* 532 (2022) 231296, <https://doi.org/10.1016/j.jpowsour.2022.231296>.

- [28] K. Kitada, O. Pecher, P.C.M.M. Magusin, M.F. Groh, R.S. Weatherup, C.P. Grey, Unraveling the reaction mechanisms of S₁₀ anodes for Li-ion batteries by combining *in situ* 7Li and *ex situ* 7Li/29Si solid-state NMR spectroscopy, *J. Am. Chem. Soc.* 141 (2019) 7014–7027, <https://doi.org/10.1021/jacs.9b01589>.
- [29] S. Li, N. Kirkaldy, C. Zhang, K. Gopalakrishnan, T. Amietszajew, L.B. Diaz, J. V. Barreras, M. Shams, X. Hua, Y. Patel, G.J. Offer, M. Marinescu, Optimal cell tab design and cooling strategy for cylindrical lithium-ion batteries, *J. Power Sources* 492 (2021) 229594, <https://doi.org/10.1016/j.jpowsour.2021.229594>.
- [30] J. Schmitt, M. Rehm, A. Karger, A. Jossen, Capacity and degradation mode estimation for lithium-ion batteries based on partial charging curves at different current rates, *J. Energy Storage* 59 (2023) 106517, <https://doi.org/10.1016/j.est.2022.106517>.